

# ARFA: AN ASYMMETRIC RECEPTIVE FIELD AUTOENCODER MODEL FOR SPATIOTEMPORAL PREDICTION

Wenxuan Zhang<sup>1,\*</sup>, Xuechao Zou<sup>1,\*</sup>, Li Wu<sup>1,†</sup>, Xiaoying Wang<sup>1</sup>, Jianqiang Huang<sup>1</sup>, Junliang Xing<sup>2</sup>

<sup>1</sup>Qinghai University, Department of Computer Technology and Applications, Xining, China

<sup>2</sup>Tsinghua University, Department of Computer Science and Technology, Beijing, China

## ABSTRACT

Spatiotemporal prediction aims to generate future sequences by paradigms learned from historical contexts. It is essential in numerous domains, such as traffic flow prediction and weather forecasting. Recently, research in this field has been predominantly driven by deep neural networks based on autoencoder architectures. However, existing methods commonly adopt autoencoder architectures with identical receptive field sizes. To address this issue, we propose an Asymmetric Receptive Field Autoencoder (ARFA) model, which introduces corresponding sizes of receptive field modules tailored to the distinct functionalities of the encoder and decoder. In the encoder, we present a large kernel module for global spatiotemporal feature extraction. In the decoder, we develop a small kernel module for local spatiotemporal information reconstruction. Experimental results demonstrate that ARFA consistently achieves state-of-the-art performance on popular datasets. Additionally, we construct the RainBench, a large-scale radar echo dataset for precipitation prediction, to address the scarcity of meteorological data in the domain.

**Index Terms**— Asymmetric receptive field, autoencoder, spatiotemporal prediction

## 1. INTRODUCTION

Spatiotemporal prediction [1], also known as video prediction, aims to synthesize temporal outputs through the input data with temporal relationships. The key is to handle the characteristics of time and space correctly. Recently, PredRNN [2, 3] has designed a new spatiotemporal LSTM (ST-LSTM) [4] unit based on RNN [5, 6, 7, 8], which memorizes spatial and temporal features in a unified memory unit and transmits memory at both vertical and horizontal levels. SimVPv2 [9, 10] has devised a GSTA structure based on the CNN [11, 12, 13, 14], architecture to effectively capture contextual features in both spatial and temporal dimensions.

Previous models, including both encoder and decoder components, have utilized modules with the same receptive field size without specific optimization, which will reduce

\*These authors contributed equally.

†Corresponding author.

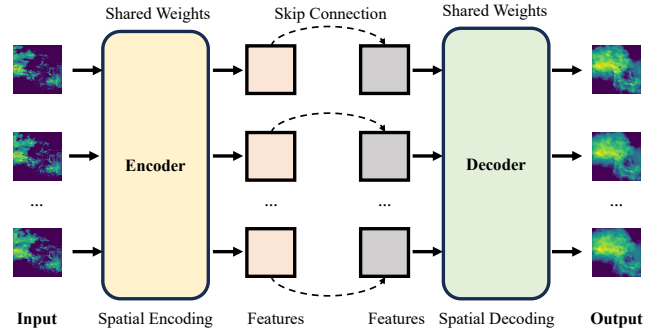


**Fig. 1.** Overall pipeline for spatiotemporal prediction using the encoder and decoder with shared weights.

the model’s accuracy for specific spatiotemporal tasks and increase computational complexity, as illustrated in Figure 1. Additionally, meteorological prediction is one of the most prevalent applications in spatiotemporal prediction, yet there is currently a lack of relevant data to support this research.

This paper proposes a novel Asymmetric Receptive Field Autoencoder (ARFA) model to address these challenges. Additionally, we constructed a large-scale precipitation prediction dataset called RainBench to tackle the missing meteorological prediction data issue.

This work mainly makes the following contributions:

- We propose a novel Asymmetric Receptive Field Autoencoder (ARFA) model that combines global encoding and local decoding to achieve high-precision spatiotemporal prediction.
- We design two novel modules for the encoder and decoder, the Large Kernel Module and the Small Kernel Module, leveraging the advantages of different-sized convolutional kernels for global spatiotemporal feature extraction and local fine structure reconstruction.
- We create a large-scale radar echo dataset for precipitation prediction, named RainBench, with the potential to serve as a benchmark for future spatiotemporal forecasting endeavors.

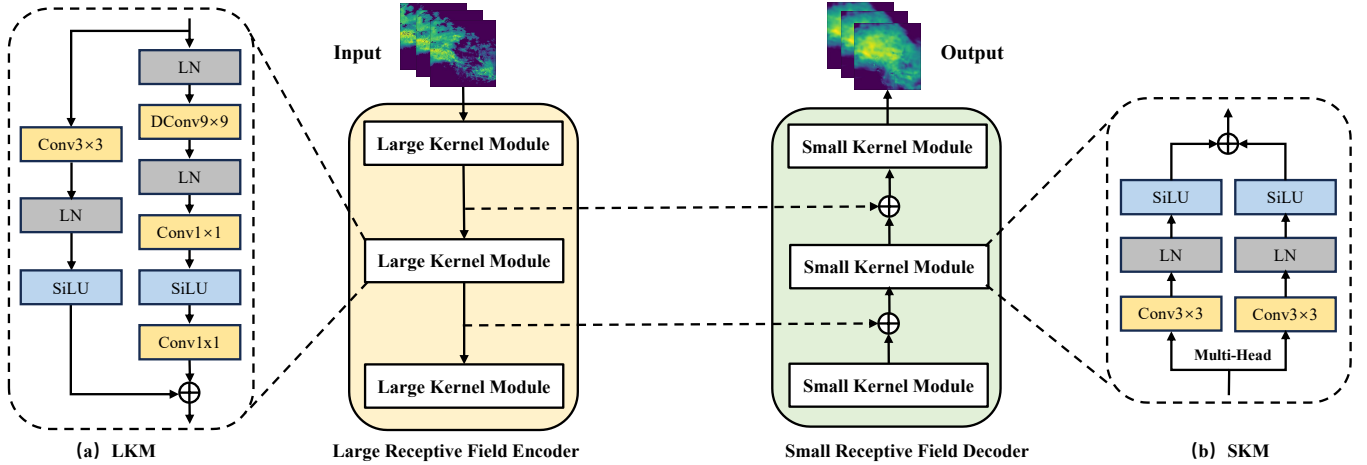


**Fig. 2.** Overall architecture of our proposed ARFA. ARFA is an autoencoder consisting of carefully designed Large Kernel Modules (LKM) and Small Kernel Modules (SKM), serving as the encoder and decoder, respectively. The LKMs offer a large receptive field for global feature extraction in the encoder, while the decoder utilizes SKMs for local information reconstruction.

## 2. ASYMMETRIC RECEPTIVE FIELD AUTOENCODER

As illustrated in Figure 2, We propose an autoencoder model with an asymmetric receptive field architecture to enhance spatiotemporal prediction accuracy, which includes the encoder and decoder of different sizes of receptive fields.

### 2.1. Encoder with Large Receptive Field

Traditional encoder architectures [15, 16] have limitations in capturing long-range dependency relationships due to their limited receptive field. We propose a novel residual structure called the Large Kernel Module (LKM) for the encoder, enabling it to capture long-range dependencies and extract more comprehensive global contextual information. Specifically, the LKM consists of two parallel branches: the main and residual branches. The main branch primarily comprises a large kernel convolution and a Multi-Layer Perceptron (MLP). The large kernel convolution employs a  $9 \times 9$  depthwise separable convolution, which incurs a small increase in parameter count to achieve a larger receptive field. Subsequently, to compensate for the performance degradation caused by the lack of channel interactions in depth-wise separable convolutions [17], we introduce an MLP composed of two  $1 \times 1$  convolutions and a SiLU [18] to recalibrate the features. Ultimately, the main branch outputs global features.

$$\mathbf{F}_{global} = \text{MLP}(\text{DConv}_{9 \times 9}(\mathbf{F}_{in})), \quad (1)$$

where  $\mathbf{F}_{in} \in \mathbb{R}^{M \times C \times H \times W}$  denotes the input features,  $M$  and  $N$  denote the lengths of the input and output temporal sequences, respectively, while  $C$ ,  $H$ , and  $W$  represent the number of channels, height, and width of a single image frame.

$\text{DConv}_{9 \times 9}$  refers to depthwise separable convolution, and  $\mathbf{F}_{global}$  represents the features outputted by the main branch of LKM.

On the other hand, the residual branch primarily consists of a convolutional layer with a  $3 \times 3$  kernel size, which facilitates the extraction of local features. Moreover, layer normalization is introduced to stabilize the training process.

$$\mathbf{F}_{local} = \sigma(\phi(\text{Conv}_{3 \times 3}(\mathbf{F}_{in}))), \quad (2)$$

where  $\sigma$  denotes the activation function,  $\phi$  refers to layer normalization, and  $\text{Conv}_{3 \times 3}$  presents standard convolution.

### 2.2. Decoder with Small Receptive Field

A smaller receptive field in the decoder is advantageous in capturing the local information of the input image more effectively, enabling the decoder to pay greater attention to details and local textures, thereby enhancing the quality of image reconstruction. Motivated by these insights, we have developed a novel Small Kernel Module (SKM), designed to leverage multi-head mechanisms [19] to augment the decoder's ability for local reconstruction.

Specifically, the SKM is a multi-head structure with two parallel branches. Each branch is composed of a  $3 \times 3$  convolution, a layer normalization, and a SiLU. Finally, the locally fine-grained features extracted from the two branches are fused through an additive operation to acquire robust features further. The specific formulation is given as follows:

$$\mathbf{F}_{out} = \sigma(\phi(\mathbf{F}_{global} + \mathbf{F}_{local})), \quad (3)$$

where  $\mathbf{F}_{out}$  denotes the output features.

**Table 1.** A comparative analysis of our RainBench dataset and two prominent spatiotemporal prediction datasets.

Dataset	Moving-MNIST [20]	KTH [21]	RainBench (Ours)
Train Sample	10,000	5,200	<b>31,600</b>
Test Sample	10,000	3,167	<b>31,600</b>
Frame Size	64×64	128×128	<b>200×200</b>
Input Length	10	10	10
Output Length	10	10	10

**Table 2.** Quantitative comparison of receptive field size.

Encoder	Decoder	MSE ↓	MAE ↓	SSIM ↑	PSNR ↑
Small	Small	27.102	78.379	0.939	38.280
Small	Large	29.973	83.104	0.932	38.114
Large	Large	28.154	78.927	0.936	38.274
<b>Large</b>	<b>Small</b>	<b>25.306</b>	<b>73.892</b>	<b>0.944</b>	<b>38.434</b>

### 3. EXPERIMENTS AND RESULTS

#### 3.1. Experimental Setup

The dataset and the implementation details are as follows.

**Dataset.** To address the data scarcity issue in the application of spatiotemporal prediction in meteorology, we have constructed a large-scale radar echo dataset called RainBench for precipitation forecasting. A comparative analysis was conducted with the mainstream spatiotemporal prediction datasets, such as Moving-MNIST [20] and KTH [21], as shown in Table 1. We collected radar echo precipitation data from the meteorological station in Yinchuan City for the months of April to October 2018 and 2019. This region is characterized not only by low precipitation amounts but also by uneven spatiotemporal distribution of precipitation. The primary precipitation features in this area include infrequent occurrence of rainfall and snowfall, as well as strong water evaporation. Consequently, spatiotemporal prediction in this region poses a significant challenge.

**Implementation Details.** The batch size for all model training is set to 16, and all experiments are conducted at 200 epochs. We employ four widely adopted metrics to evaluate on the test set: MSE, MAE, PSNR, and SSIM [22].

#### 3.2. Ablation and Analysis

To validate the effectiveness of our proposed asymmetric receptive field autoencoder model, we conduct four sets of ablation experiments on the most popular Moving-MNIST dataset, and the results are presented in Table 2 and Table 3.

**Asymmetric Receptive Field in the Autoencoder.** As shown in Table 2, in the design of the autoencoder, the optimal combination for achieving the best performance is to employ a large receptive field in the encoder and a small receptive field in the decoder.

**Convolutional Kernel Size in the LKM.** The size of the

**Table 3.** Ablation of convolution kernel size in the LKM.

Kernel Size	MSE ↓	MAE ↓	SSIM ↑	PSNR ↑
3×3	26.605	76.354	0.940	38.361
5×5	26.102	75.495	0.941	38.383
7×7	26.004	75.278	0.941	38.385
<b>9×9</b>	<b>25.975</b>	<b>74.783</b>	<b>0.942</b>	<b>38.398</b>
11×11	25.999	75.265	0.942	38.366

**Table 4.** Quantitative comparison on the Moving-MNIST.

Method	MSE ↓	MAE ↓	SSIM ↑	PSNR ↑
ConvLSTM [23]	34.071	97.250	0.919	37.614
PhyDNet [6]	28.207	78.501	0.937	38.133
MAU [5]	26.842	78.049	0.940	38.197
PredRNN [2]	33.472	95.148	0.917	37.792
PredRNN++ [3]	50.374	108.13	0.904	37.978
E3DLSTM [7]	44.652	83.778	0.924	39.749
PredRNNv2 [24]	27.730	80.840	0.937	38.293
SimVPv1 [9]	32.203	89.291	0.927	37.951
SimVPv2 [10]	27.102	78.379	0.939	38.280
<b>ARFA (Ours)</b>	<b>25.306</b>	<b>73.892</b>	<b>0.944</b>	<b>38.434</b>

convolutional kernel in the LKM directly influences the encoder’s receptive field. Table 3 demonstrates that as the kernel size increases, the encoder exhibits more effective feature extraction with the support of a larger receptive field. Further increasing the kernel size leads to a performance decline.

#### 3.3. Comparison with the State-of-the-Arts

We conduct extensive experiments to quantitatively and qualitatively compare the performance of our proposed method, ARFA, with existing methods for spatiotemporal prediction on two popular datasets, Moving-MNIST and KTH, and on our custom-built RainBench dataset.

**Moving-MNIST.** Table 4 shows the quantitative comparison results of our ARFA and existing approaches on the Moving-MNIST dataset. ARFA achieves state-of-the-art (SOTA) performance consistency across four evaluation metrics. Compared to SimVPv2, ARFA exhibits reductions of 1.796 and 4.487 in MSE and MAE. As shown in Figure 3 (a), it can be observed that ARFA consistently generates high-fidelity images. In contrast, other models, such as SimVPv2, PredRNN, and ConvLSTM, suffer from image blurring, while PredRNN exhibits semantic inconsistencies.

**KTH.** Table 5 shows the quantitative comparison results of our proposed ARFA method and existing approaches on the KTH dataset. ARFA achieves SOTA performance in terms of four evaluation metrics. Compared to SimVPv2, ARFA demonstrates a reduction of 4.650 and 59.431 in terms of MSE and MAE. As depicted in Figure 3 (b), it can be observed that SimVPv2 fails to restore the arm of the person, and the generated result by ConvLSTM fails to predict the

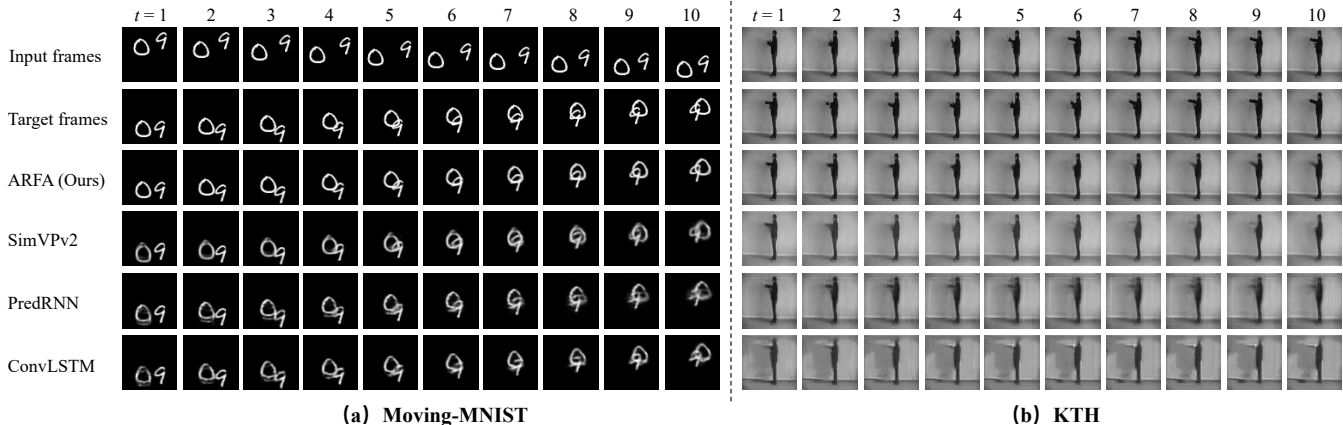


Fig. 3. Visual results of our ARFA and existing methods on the Moving-MNIST and KTH dataset.

Table 5. Quantitative comparison on the KTH dataset.

Method	MSE ↓	MAE ↓	SSIM ↑	PSNR ↑
ConvLSTM [23]	65.164	588.333	0.855	31.215
PredRNN [2]	60.897	515.372	0.867	32.383
SimVPv2 [10]	47.541	463.063	0.903	32.740
<b>ARFA (Ours)</b>	<b>42.891</b>	<b>403.632</b>	<b>0.907</b>	<b>33.667</b>

Table 6. Quantitative comparison on the RainBench dataset.

Method	MSE ↓	MAE ↓	SSIM ↑	PSNR ↑
ConvLSTM [23]	132.936	976.618	0.797	35.737
PredRNN [2]	128.589	877.229	0.829	36.833
PredRNN++ [3]	119.671	956.249	0.795	35.710
MIM [8]	119.654	874.465	0.785	34.992
SimVPv2 [10]	112.383	826.336	0.834	36.732
<b>ARFA (Ours)</b>	<b>109.880</b>	<b>809.190</b>	<b>0.842</b>	<b>36.844</b>

head and arms. In contrast, images generated by ARFA exhibit no such blurriness or semantic inconsistencies.

**RainBench.** Table 6 shows the quantitative comparison results of our ARFA and existing approaches on our RainBench dataset. ARFA achieves SOTA performance consistency across four evaluation metrics. Compared to SimVPv2, ARFA reduces the MSE by 2.503 and the MAE by 17.146. Moreover, ARFA exhibits improvements in SSIM and PSNR. As depicted in Figure 4, it can be observed that ARFA consistently outperforms other methods in terms of prediction accuracy. Given the inherent challenges of the dataset, future research endeavors could employ RainBench as a benchmark to further explore superior spatiotemporal prediction algorithms. SimVPv2 follows as the second-best performer. However, alternative methods such as MIM, PredRNN, and ConvLSTM gradually lose the original characteristics of the generated images as the prediction time steps increase.

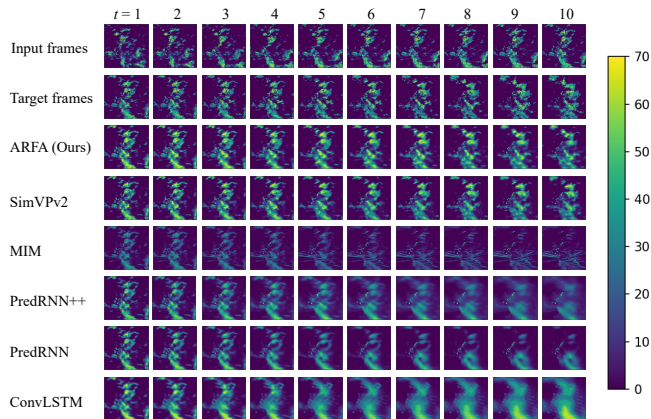


Fig. 4. A visual comparison on the RainBench dataset.

## 4. CONCLUSION

This work presents an Asymmetric Receptive Field Autoencoder model to handle spatiotemporal correlations in spatiotemporal prediction. Additionally, RainBench, a large-scale dataset specific to the characteristics of China, is constructed for precipitation prediction. Experimental results confirm the effectiveness of our proposed ARFA. The source code and dataset will be released to facilitate further research.

## 5. ACKNOWLEDGE

This paper is supported by the National Natural Science Foundation of China (No. 62162053, No. 42265010, No. 62222606, and No. 62076238) and the Natural Science Foundation of Qinghai Province (2023-ZJ-906M).

## References

- [1] Alex Graves and Jürgen Schmidhuber, “Framewise phoneme classification with bidirectional lstm and other neural network architectures,” *NEURAL NETWORKS*, vol. 18, no. 5-6, pp. 602–610, 2005.
- [2] Yunbo Wang, Mingsheng Long, Jianmin Wang, Zhifeng Gao, and Philip S Yu, “Predrnn: Recurrent neural networks for predictive learning using spatiotemporal lstms,” *NeurIPS*, vol. 30, 2017.
- [3] Yunbo Wang, Zhifeng Gao, Mingsheng Long, Jianmin Wang, and S Yu Philip, “Predrnn++: Towards a resolution of the deep-in-time dilemma in spatiotemporal predictive learning,” in *ICML*, 2018, pp. 5123–5132.
- [4] Sepp Hochreiter and Jürgen Schmidhuber, “Long short-term memory,” *NEURAL COMPUT*, vol. 9, no. 8, pp. 1735–1780, 1997.
- [5] Zheng Chang, Xinfeng Zhang, Shanshe Wang, Siwei Ma, Yan Ye, Xiang Xinguang, and Wen Gao, “Mau: A motion-aware unit for video prediction and beyond,” *NeurIPS*, vol. 34, pp. 26950–26962, 2021.
- [6] Vincent Le Guen and Nicolas Thome, “Disentangling physical dynamics from unknown factors for unsupervised video prediction,” in *CVPR*, 2020, pp. 11474–11484.
- [7] Yunbo Wang, Lu Jiang, Ming-Hsuan Yang, Li-Jia Li, Mingsheng Long, and Li Fei-Fei, “Eidetic 3d lstm: A model for video prediction and beyond,” in *ICLR*, 2018.
- [8] Yunbo Wang, Jianjin Zhang, Hongyu Zhu, Mingsheng Long, Jianmin Wang, and Philip S Yu, “Memory in memory: A predictive neural network for learning higher-order non-stationarity from spatiotemporal dynamics,” in *CVPR*, 2019, pp. 9154–9162.
- [9] Zhangyang Gao, Cheng Tan, Lirong Wu, and Stan Z Li, “Simvp: Simpler yet better video prediction,” in *CVPR*, 2022, pp. 3170–3180.
- [10] Cheng Tan, Zhangyang Gao, Siyuan Li, and Stan Z. Li, “Simvp: Towards simple yet powerful spatiotemporal predictive learning,” 2023.
- [11] Weibin Zhang, Yinghao Yu, Yong Qi, Feng Shu, and Yinhai Wang, “Short-term traffic flow prediction based on spatio-temporal analysis and cnn deep learning,” *TRANSPORTMETRICA A*, vol. 15, no. 2, pp. 1688–1711, 2019.
- [12] William Robert Johnson, Jacqueline Alderson, David Lloyd, and Ajmal Mian, “Predicting athlete ground reaction forces and moments from spatio-temporal driven cnn models,” *TBME*, vol. 66, no. 3, pp. 689–694, 2018.
- [13] Xuechao Zou, Kai Li, Junliang Xing, Yu Zhang, Shiyang Wang, Lei Jin, and Pin Tao, “Differ: A fast conditional diffusion framework for cloud removal from optical satellite images,” 2023.
- [14] Xiaolin Hu, Kai Li, Weiyi Zhang, Yi Luo, Jean-Marie Lemercier, and Timo Gerkmann, “Speech separation using an asynchronous fully recurrent convolutional neural network,” in *NeurIPS*, 2021, vol. 34, pp. 22509–22522.
- [15] Xuechao Zou, Kai Li, Junliang Xing, Pin Tao, and Yachao Cui, “Pmaa: A progressive multi-scale attention autoencoder model for high-performance cloud removal from multi-temporal satellite imagery,” 2023.
- [16] Kai Li, Runxuan Yang, and Xiaolin Hu, “An efficient encoder-decoder architecture with top-down attention for speech separation,” in *ICLR*, 2023.
- [17] Andrew G. Howard, Menglong Zhu, Bo Chen, Dmitry Kalenichenko, Weijun Wang, Tobias Weyand, Marco Andreetto, and Hartwig Adam, “Mobilenets: Efficient convolutional neural networks for mobile vision applications,” 2017.
- [18] Stefan Elfving, Eiji Uchibe, and Kenji Doya, “Sigmoid-weighted linear units for neural network function approximation in reinforcement learning,” *NEURAL NETWORKS*, vol. 107, pp. 3–11, 2018.
- [19] Ashish Vaswani, Noam Shazeer, Niki Parmar, Jakob Uszkoreit, Llion Jones, Aidan N Gomez, Lukasz Kaiser, and Illia Polosukhin, “Attention is all you need,” *NeurIPS*, vol. 30, 2017.
- [20] Kiran Kumar Chandriah and Raghavendra V Naragana-halli, “Rnn/lstm with modified adam optimizer in deep learning approach for automobile spare parts demand forecasting,” *MULTIMED TOOLS APPL*, vol. 80, no. 17, pp. 26145–26159, 2021.
- [21] Lena Gorelick, Moshe Blank, Eli Shechtman, Michal Irani, and Ronen Basri, “Actions as space-time shapes,” *TPAMI*, vol. 29, no. 12, pp. 2247–2253, 2007.
- [22] Alain Hore and Djemel Ziou, “Image quality metrics: Psnr vs. ssim,” in *ICPR*, 2010, pp. 2366–2369.
- [23] Xingjian Shi, Zhouong Chen, Hao Wang, Dit-Yan Yeung, Wai-Kin Wong, and Wang-chun Woo, “Convolutional lstm network: A machine learning approach for precipitation nowcasting,” *NeurIPS*, vol. 28, 2015.
- [24] Yunbo Wang, Haixu Wu, Jianjin Zhang, Zhifeng Gao, Jianmin Wang, S Yu Philip, and Mingsheng Long, “Predrnn: A recurrent neural network for spatiotemporal predictive learning,” *TPAMI*, vol. 45, no. 2, pp. 2208–2225, 2022.